Supplements to: Dissolved Mn(III) is a key redox intermediate in sediments of a seasonally euxinic coastal basin

1. Detailed model description

The reactions in the model describe organic matter (OM) degradation involving a range of electron acceptors combined with secondary reactions of the reaction products (Table S5). Degradation of OM is facilitated, in successive order, by reduction of O_2, NO_3^-, MnO_2, $Fe(OH)_3$ and SO_4^{2-} and finally OM is degraded via methanogenesis (Table S2; Froelich et al., 1979; Reed et al., 2011; Rooze et al., 2016). Monod kinetics are used to describe the sequence of electron acceptors in OM degradation (Boudreau, 1997). In Monod kinetics, the oxidant with the highest metabolic free energy yield is used preferentially, until this species becomes limiting and the next oxidant in the sequence is used preferentially (Boudreau, 1996; Van Cappellen & Wang, 1996). The OM is assumed to include carbon (C), nitrogen (N) and phosphorus (P) in a ratio of C:N:P = 106:15.45:1 (based on Egger et al., 2016b). In the model, reduction of MnO_2 can be coupled to oxidation of OM, Fe(II), H_2S and CH_4 (Table S2). Reduction of MnO_2 by OM, Fe(II) and H_2S is modelled as one electron transfer steps with Mn(III) as the product (Madison et al., 2013). Reduction of MnO_2 by CH_4 is modelled as a two electron transfer with Mn(II) as a product, because, to our knowledge, the one electron transfer step that is theoretically possible has never been demonstrated. Reduction of Mn(III) is assumed to occur with Fe(II), H_2S and OM to form Mn(II), while oxidation of Mn(III) is assumed to occur with O_2 to form MnO_2. Oxidation of Mn(II) with O_2 and precipitation as $MnCO_3$ removes Mn(II). Dissolved inorganic carbon in the model is the sum of carbon in HCO_3^{2-} and CO_2, which are produced or consumed in reactions.

Depending on whether a compound is a solid or solute, its generic mass conservation is described by Eq. 1 or Eq. 2, respectively.

$$(1 - \varphi)\frac{\partial C_s}{\partial t} = -(1 - \varphi)v\frac{\partial C_s}{\partial z} + \sum R_s \quad (1)$$

$$\varphi\frac{\partial C_{aq}}{\partial t} = \varphi D'\frac{\partial^2 C_{aq}}{\partial z^2} - \varphi u\frac{\partial C_{aq}}{\partial z} + \sum R_{aq} \quad (2)$$

In these equations, φ is the sediment porosity, t is time (yr), C_s and C_{aq} are the concentrations of the solid and dissolved species (mol L^{-1}), respectively, D' is the diffusion coefficient of dissolved species in the porous medium (cm^2 yr^{-1}), z is the distance from the Sediment-Water Interface (SWI; cm), v and u (cm yr^{-1}) are advective velocities of solids and dissolved species, respectively and ΣR_s and ΣR_{aq} are net rates of chemical reactions of solid and dissolved species, respectively.

For porosity, a depth-dependent function is used to account for sediment compaction (Meysman et al., 2005; Reed 2011a) (eq 3):

$$\varphi(x) = \varphi_\infty + (\varphi_0 - \varphi_\infty)e^{-\frac{y}{x}} \quad (3)$$

In this equation, φ_0 is the porosity at the SWI, φ_∞ is the porosity at depth and y is the porosity attenuation factor/e-folding distance (Table 3).

In the last 20 years of the model run, the seasonal cycle of oxic – euxinic conditions was simulated by varying the bottom water O_2 and H_2S concentration, the influx of Fe oxides, Mn oxides and OM and the sedimentation rate (Fig. S1). The boundary conditions for the bottom water concentration of O_2 were based on monitoring by Rijkswaterstaat (Directorate-General for Public Works and Water Management of the Netherlands) as reported in Żygadłowska et al. (2023a). The bottom water H_2S was varied together with O_2 and was either 0, or the concentration measured in the bottom water in September (111.8 μM). Input of metal oxides was varied together with O_2 and was fitted to the sediment profiles. OM input was varied to fit the sediment profiles. The input of OM and the sedimentation rate in April differ from those in the other oxic months, because a spring bloom is simulated. Sedimentation rates for the model run until 2014 (6 years before the end of the model) were based on Egger et al. (2016; 13.3 cm yr^{-1}). For the last 6 years the sedimentation rate was set to 20 cm yr^{-1}, based on the onset of the shallowest peak in C_{org} at 20 cm depth (Fig. 4), which marks the C_{org} deposition of the previous year (i.e. spring 2019).

2. Figures

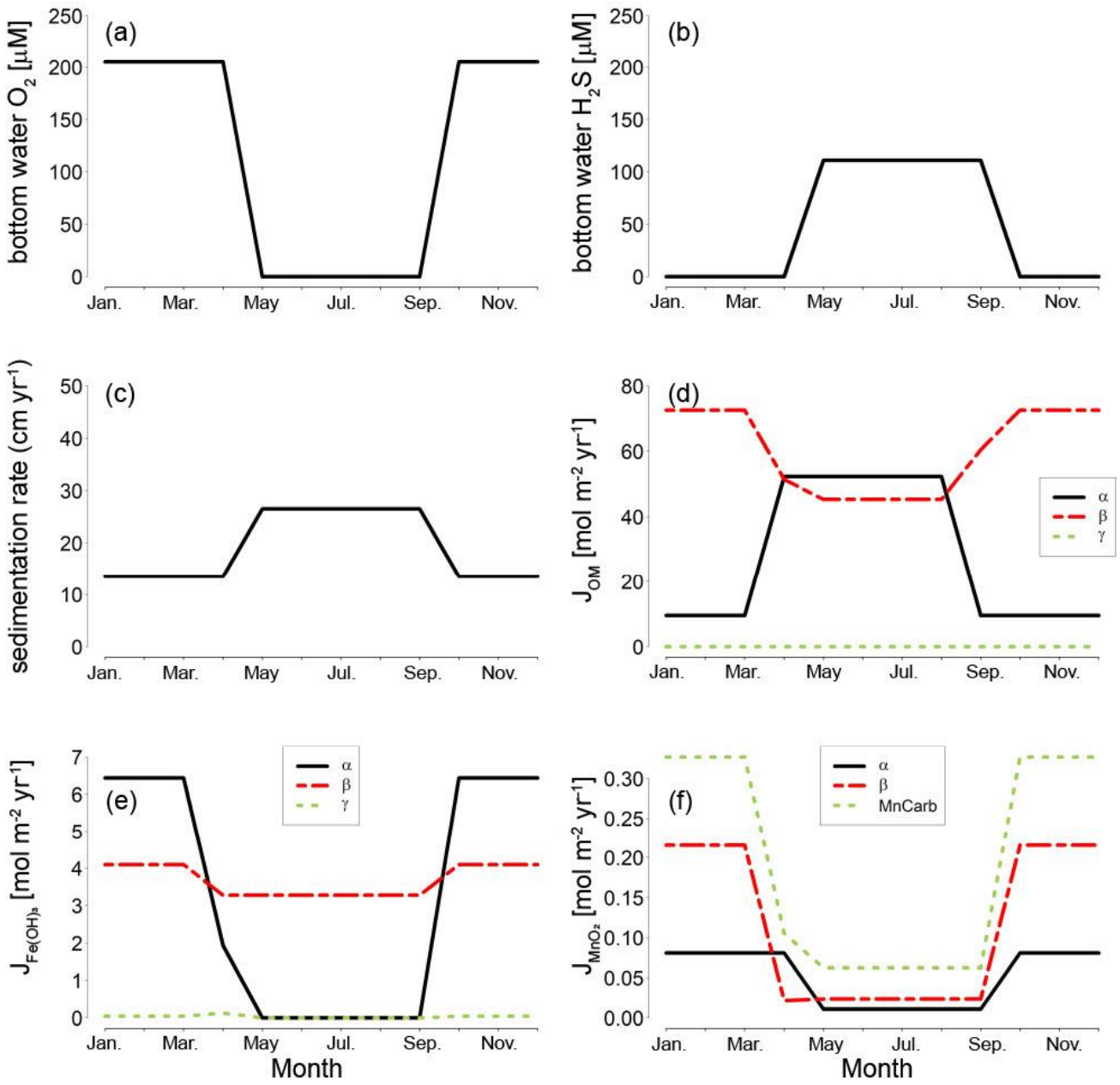

Figure S1. Seasonal variation in bottom water O_2 and H_2S, sedimentation rate, and in the flux of Fe oxides ($J_{Fe(OH)_3}$), flux of Mn oxides (J_{MnO_2}) and flux of organic matter (J_{OM}) at the sediment-water interface in the final year of the model simulations.

45

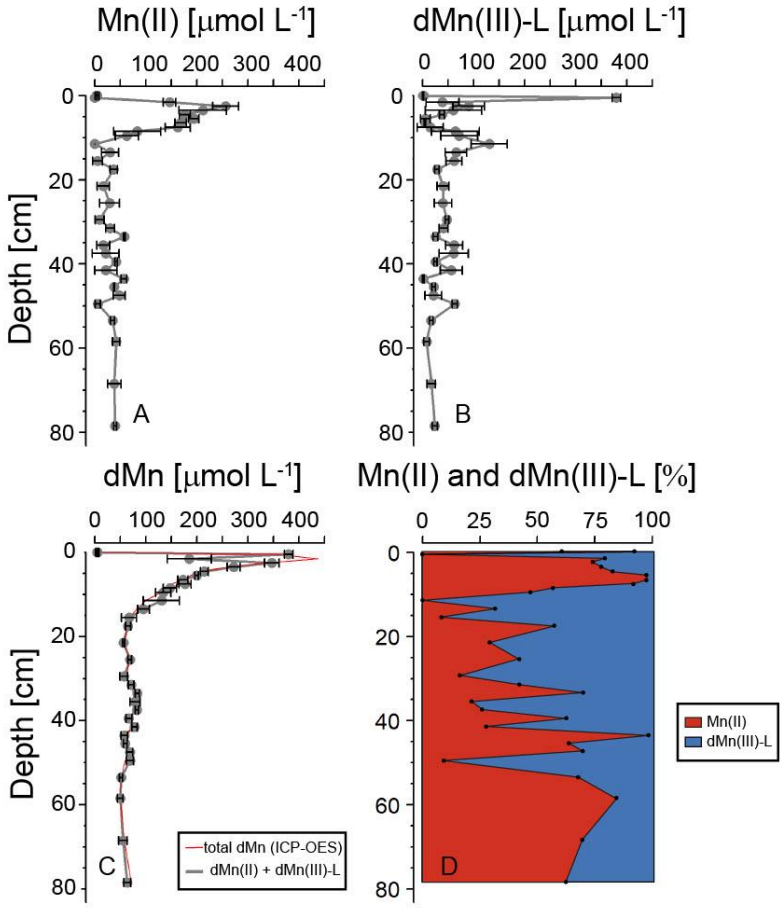

Figure S2: A, B) Data collected through spectrophotometric analysis of Mn(II) and dMn(III)-L in March, including error bars showing standard deviation (n=3). C) The sum of Mn(II) and dMn(III)-L measured spectrophotometrically, including error bars showing standard deviation (n=3), compared with the total dissolved Mn measured with ICP-OES. D) The contribution of Mn(II) and dMn(III)-L to the total dissolved Mn pool (determined as the sum of Mn(II) and dMn(III)-L) as percentage.

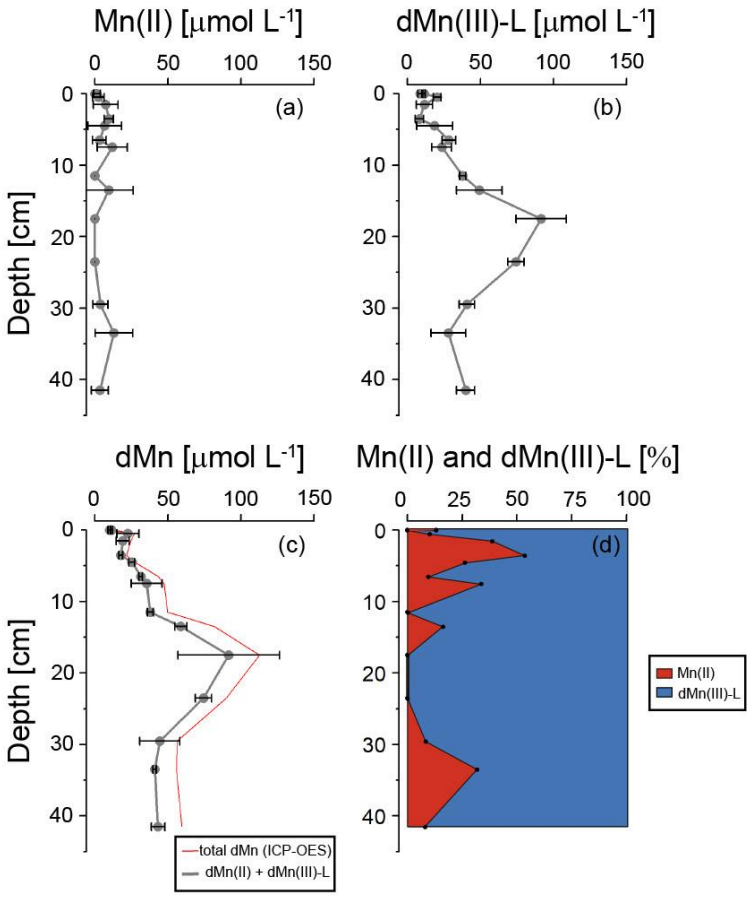

Figure S3: A, B) Data collected during the spectrophotometric analysis of Mn(II) and dMn(III)-L in September, including error bars showing standard deviation (n = 3). C) The sum of Mn(II) and dMn(III)-L measured during the spectrophotometric method including error bars (n = 3), compared with the total dissolved Mn measured with ICP-OES. D) The contribution of Mn(II) and dMn(III)-L to the total dissolved Mn pool (determined as the sum of Mn(II) and dMn(III)-L) as a percentage.

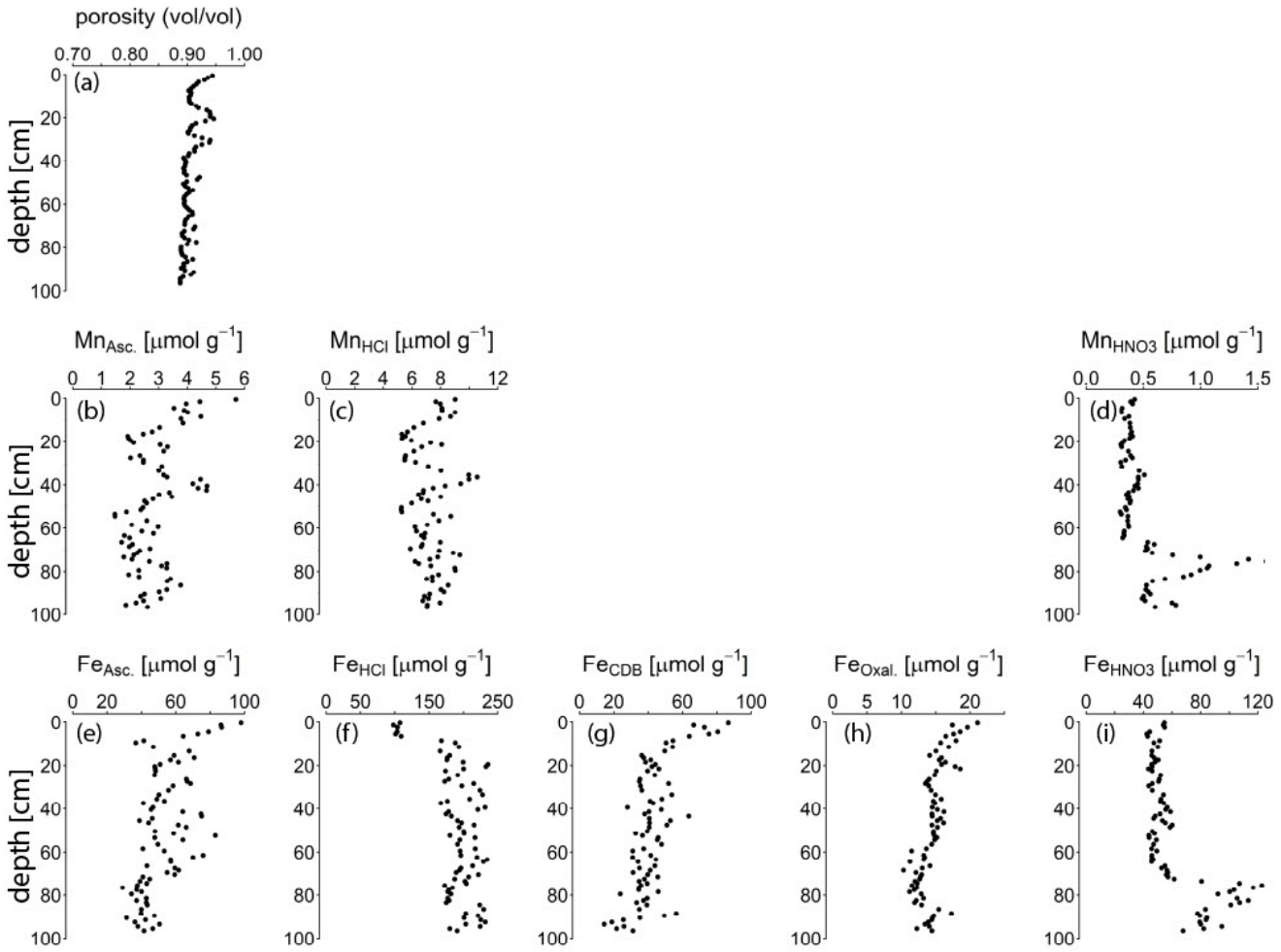

Figure S4: Porosity and all Mn and Fe fractions as determined in the sequential extraction, for the sediment collected in March 2020.

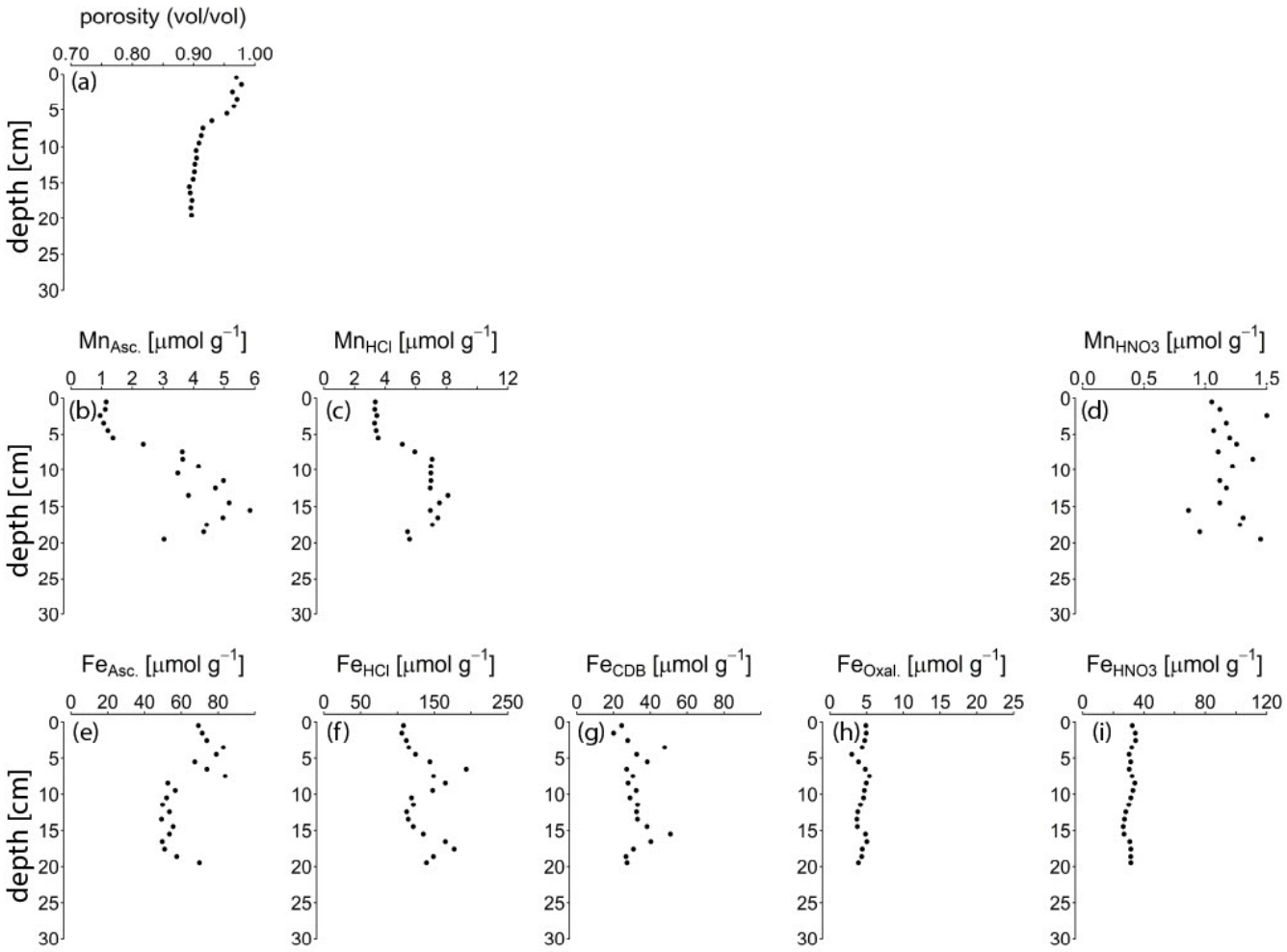

Figure S5: Porosity and all fractions extracted for Mn and Fe in the sequential extraction, for the sediment collected in September 2020 (0-20 cm).

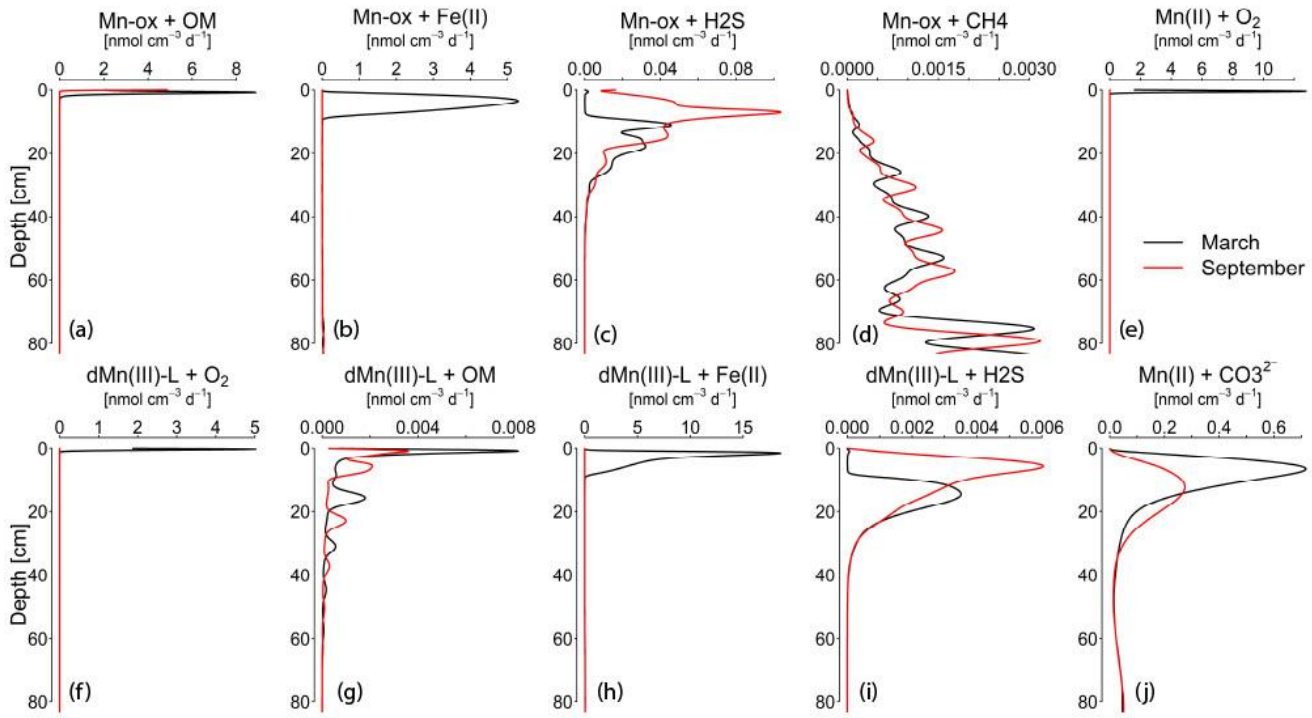

Figure S6: Depth profiles of the reaction rates, which form the basis for the rate integrations shown in Fig. 4.

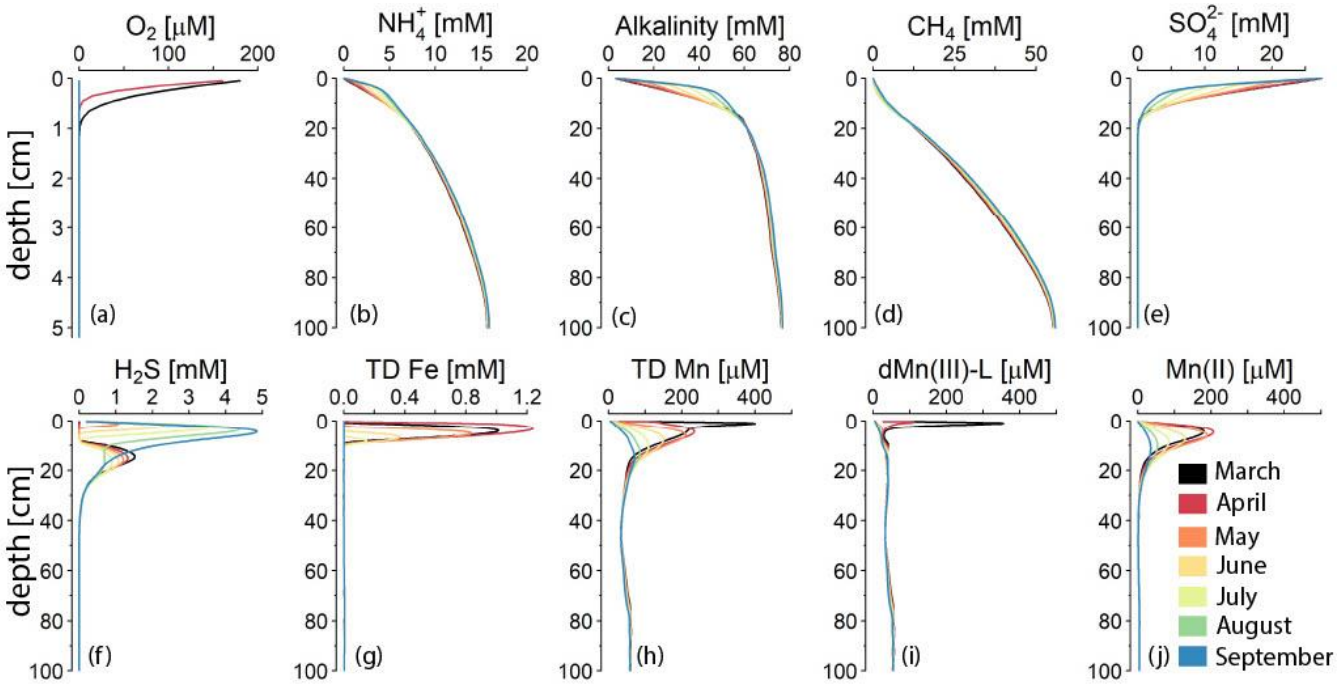

70 **Figure S7. The change in pore water profiles between March and September when anoxic conditions develop in the basin. With the reactive transport model, pore water profiles can be extrapolated to months where no fieldwork was done.**

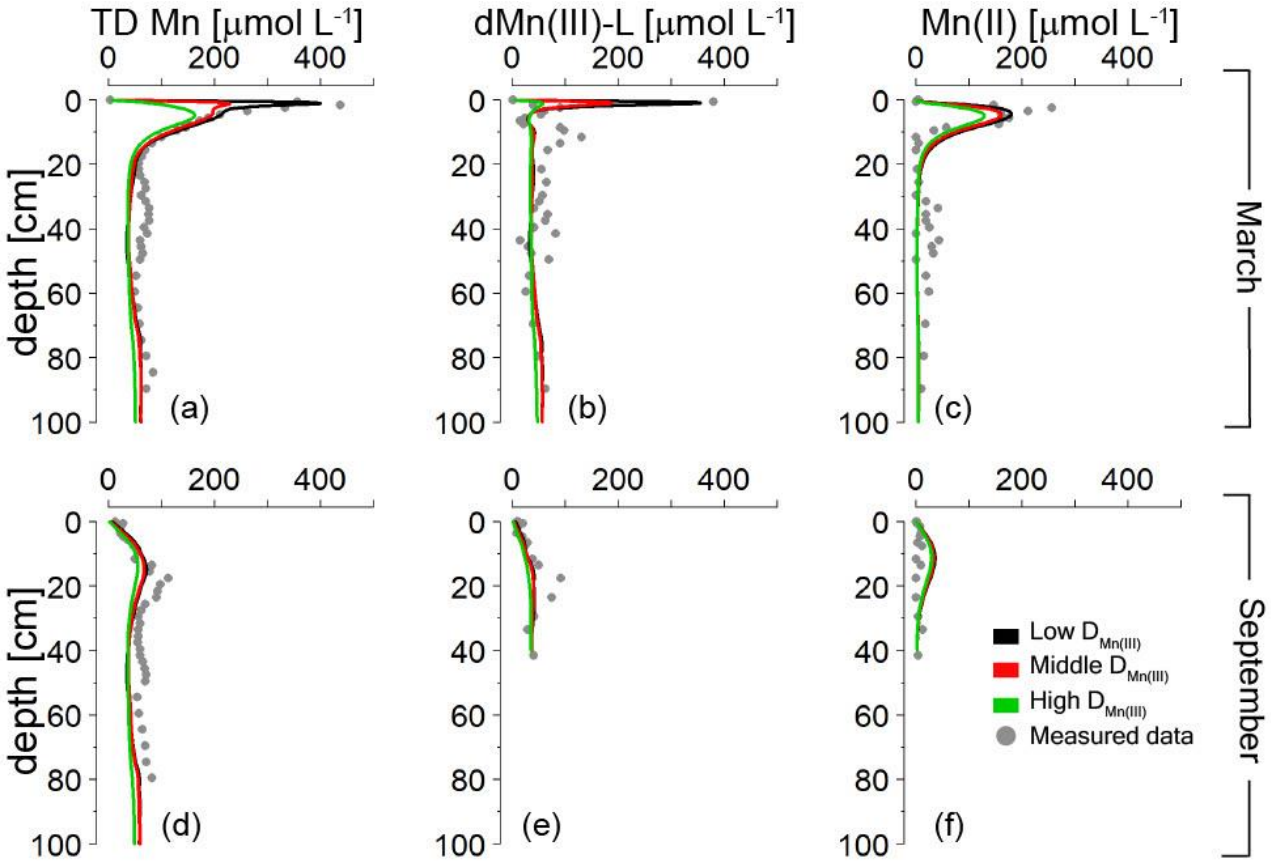

Figure S8: Model runs with different diffusion coefficients for dissolved Mn(III). The diffusion coefficients used and the range of diffusion coefficients for dissolved organic matter given in literature can be found in Table S6. When the diffusion coefficient decreases, the peak of dissolved Mn(III)-L and total dissolved Mn near the sediment-water interface in March is no longer well described by the model. The diffusion coefficient does not have a large effect on the pore water profiles of Mn(II) and dMn(III)-L in September.

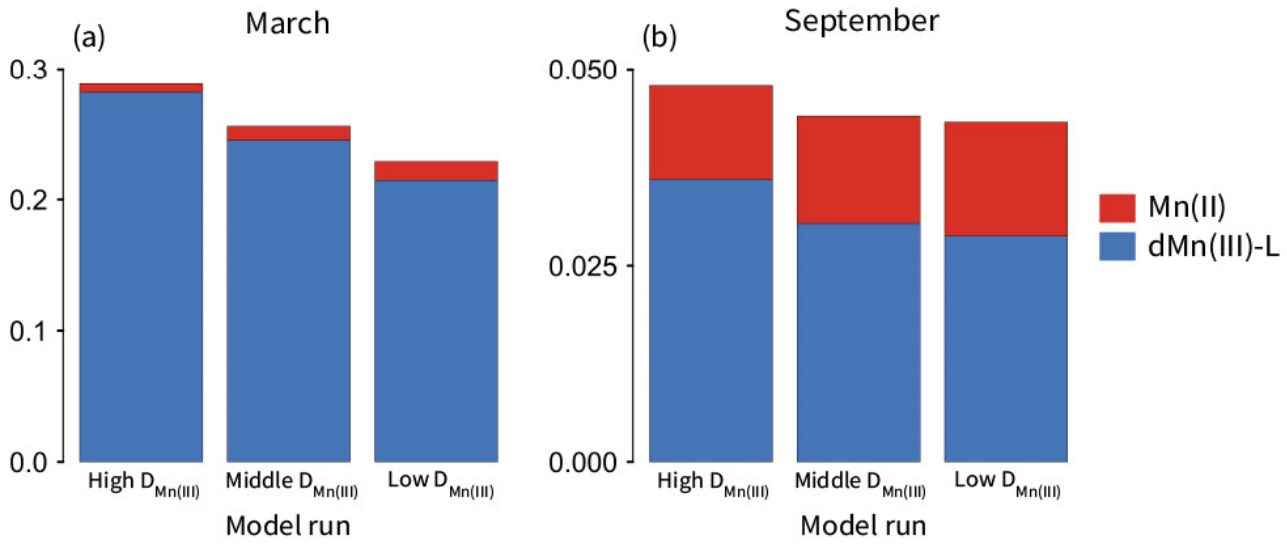

Figure S9: Variation in the benthic flux of dissolved Mn over the model runs with changing diffusion coefficient for dMn(III)-L ($D_{Mn(III)}$) in March (A) and September (B). Note the different y-axes for the different months. The figure shows that a lower diffusion coefficient for dMn(III)-L results in a lower benthic flux of total Mn and dMn(III)-L, but a slightly higher benthic flux of Mn(II). The values for the high, middle and low $D_{Mn(III)}$ can be found in Table S6.

3. Tables

Table S1. Chemical species included in the model

Species	Notation
Solids	
Organic Matter[a]	$OM^{\alpha/\beta/\gamma}$
Iron oxides[a]	$Fe(OH)_3^{\alpha/\beta/\gamma}$
Iron monosulfide	FeS
Pyrite	FeS_2
Elemental Sulfur	S^0
Siderite	$FeCO_3$
Vivianite	$Fe_3(PO_4)_2$
Manganese oxide[b]	$MnO_2^{\alpha/\beta}$
Manganese carbonate	$MnCO_3$
Solutes	
Chloride	Cl^-
Oxygen	O_2
Nitrate	NO_3^-
Sulfate	SO_4^{2-}
Methane	CH_4
Dissolved iron	Fe^{2+}
Ammonium[c]	ΣNH_4^+
Hydrogen sulfide[c]	ΣH_2S
Phosphate[c]	ΣH_3PO_4
Dissolved Inorganic Carbon	DIC
Dissolved manganese (II)	Mn^{2+}
Dissolved manganese(III)-L	Mn^{3+}

[a] Consists of three types of species: reactive (α), less reactive (β) and non-reactive (γ)

[b] Consists of two types of species: reactive (α) and less reactive (β)

[c] Σ denotes that all species of an acid are included.

Table S2. Reaction pathways and stoichiometries implemented in the model

Primary redox reactions

$OM^{\alpha,\beta} + a\ O_2 \rightarrow a\ CO_2 + b\ NH_4^+ + c\ H_3PO_4 + a\ H_2O$	R1
$OM^{\alpha,\beta} + 0.8\ a\ NO_3 + 0.8\ a\ H^+ \rightarrow a\ CO_2 + b\ NH_4^+ + c\ H_3PO_4 + 0.4\ a\ N_2 + 1.4\ a\ H_2O$	R2
$OM^{\alpha,\beta} + 4a\ MnO_2{}^a + 2\ a\ H^+ \rightarrow 4a\ Mn^{3+} + a\ CO_2 + b\ NH_4^+ + c\ H_3PO_4 + 2\ a\ H_2O$	R3
$OM^{\alpha,\beta} + 4a\ Fe(OH)_3{}^a + 4a\ \chi\ Fe_{ox}P + 12\ a\ H^+ \rightarrow 4a\ Fe^{2+} + a\ CO_2 + b\ NH_4^+ + (c + 4a\ \chi)H_3PO_4 + 13a\ H_2O$	R4
$OM^{\alpha,\beta} + 0.5a\ SO_4{}^{2-} + a\ H^+ \rightarrow a\ CO_2 + b\ NH_4^+ + c\ H_3PO_4 + 0.5a\ H_2S + a\ H_2O$	R5
$OM^{\alpha,\beta} \rightarrow 0.5a\ CO_2 + b\ NH_4^+ + c\ H_3PO_4 + 0.5a\ CH_4$	R6

Secondary and other reactions

$O_2 + Fe^{2+} + 8\ H_2O + 4\ \chi\ H_3PO_4 \rightarrow 4\ Fe(OH)_3{}^a + 4\ \chi\ Fe_{ox}P + 8\ CO_2$	R7
$2\ O_2 + FeS \rightarrow SO_4^{2-} + 2\ Fe^{2+} + 4\ H^+$	R8
$7\ O_2 + 2\ FeS_2 + 2\ H_2O + 4\ SO_4^{2-} \rightarrow 2\ Fe^{2+} + 4\ H^+$	R9
$2\ O_2 + H_2S + 2\ HCO_3^- \rightarrow SO_4^{2-} + 2\ CO_2 + 2\ H_2O$	R10
$2\ O_2 + CH_4 \rightarrow CO_2 + 2\ H_2O$	R11
$2\ Fe(OH)_3{}^a + 2\ \chi\ Fe_{ox}P + H_2S + 4\ CO_2 \rightarrow 2\ Fe^{2+} + 2\ \chi H_2PO_4{}^- + S^0 + 4\ HCO_3^- + 2\ H_2O$	R12
$Fe^{2+} + H_2S \rightarrow FeS + 2\ H^+$	R13
$FeS + H_2S \rightarrow FeS_2 + H_2$	R14
$SO_4^{2-} + CH_4 + CO_2 \rightarrow 2\ HCO_3^- + H_2S$	R15
$CH_4 + 8\ Fe(OH)_3{}^{a,\beta} + 8\ \chi\ Fe_{ox}P + 15\ H^+ \rightarrow HCO_3^- + 8\ Fe^{2+} + 8\ \chi H_2PO_4{}^- + 21\ H_2O$	R16
$4\ S^0 + 4\ H_2O \rightarrow 3\ H_2S + SO_4^{2-} + 2\ H^+$	R17
$FeS + S^0 \rightarrow FeS_2$	R18
$Fe(OH)_3{}^a + \chi\ Fe_{ox}P \rightarrow Fe(OH)_3{}^\beta + \chi\ H_2PO_4{}^-$	R19
$2\ Fe(OH)_3{}^\beta + 2\ \chi\ Fe_{ox}P + H_2S + 4\ CO_2 \rightarrow 2\ Fe^{2+} + 2\ \chi\ H_2PO_4{}^- + S^0 + 4\ HCO_3^- + 2\ H_2O$	R20
$2\ O_2 + NH_4^+ + 2\ HCO_3^- \rightarrow NO_3^- + 2\ CO_2 + 3\ H_2O$	R21
$3\ Fe^{2+} + 2\ H_2PO_4{}^- \rightarrow Fe_3(PO_4)_2 + 4\ H^+$	R22
$Fe^{2+} + CO_3{}^{2-} \rightarrow FeCO_3$	R23
$FeCO_3 + H_2S \rightarrow FeS + CO_2 + H_2O$	R24
$Fe_3(PO_4)_2 + 3\ H_2S \rightarrow 2\ FeS + 2\ HPO_4^- + 4\ H^+$	R25
$Mn^{2+} + HCO_3^- + OH^- \rightarrow MnCO_3 + H_2O$	R26
$4\ Mn^{2+} + O_2 + 4\ H^+ + L \rightarrow 4\ Mn^{3+} - L + 2\ H_2O$	R27

$MnO_2{}^{a,\beta} + Fe^{2+} + H_2O + H^+ + L \rightarrow Fe(OH)_3{}^{a} + Mn^{3+} - L$	R28
$MnO_2{}^{a} + H_2S + + 2\,H^+ + L \rightarrow S^0 + Mn^{3+} - L + 2\,H_2O$	R29
$MnO_2{}^{a} \rightarrow MnO_2{}^{\beta}$	R30
$MnO_2{}^{\beta} + H_2S + + 2\,H^+ + L \rightarrow S^0 + Mn^{3+} - L + 2\,H_2O$	R31
$4\,MnO_2{}^{a,\beta} + CH_4 + 7\,H^+ \rightarrow 4\,Mn^{2+} + HCO_3^- + 5\,H_2O$	R32
$4\,Mn^{3+} - L + 2\,O_2 + 4\,H^+ \rightarrow 4\,MnO_2{}^{a} + 2\,H_2O + L$	R33
$Mn^{3+} - L + H_2S \rightarrow S^0 + Mn^{2+} + L$	R34
$Mn^{3+} - L + Fe^{2+} + 3\,H_2O \rightarrow Mn^{2+} + Fe(OH)_3{}^{a} + 3\,H^+ + L$	R35
$4\,Mn^{3+} - L + OM^{\alpha} + H_2O \rightarrow 4\,Mn^{2+} + CO_2 + 3\,H^+ + L$	R36

Organic matter is of the form $((CH_2O)_a (NH_4{}^+)_b (H_3PO_4)_c$, where a=1, b= 1/15.45 and c = 106/1. α, β, & γ describe different fractions (i.e. highly reactive, less reactive and refractory). χ describes the P:Fe ratios of $Fe(OH)_3$ and has a value of 0.3 in the model.

Table S3. Reaction equations implemented in the model

Primary redox reaction equations	
R1 = $k_{\alpha,\beta}\ OM^{\alpha,\beta}\ \left(\frac{[O_2]}{K_{m,O_2}+[O_2]}\right)$	E1
R2 = $k_{\alpha,\beta}\ OM^{\alpha,\beta}\ \left(\frac{[NO_3^-]}{K_{m,NO_3^-}+[NO_3^-]}\right)\left(\frac{[O_2]}{K_{m,O_2}+[O_2]}\right)$	E2
R3 = $k_{\alpha,\beta}\ OM^{\alpha,\beta}\ \left(\frac{[MnO_2]}{K_{m,MnO_2}+[MnO_2]}\right)\left(\frac{[NO_3^-]}{K_{m,NO_3^-}+[NO_3^-]}\right)\left(\frac{[O_2]}{K_{m,O_2}+[O_2]}\right)$	E3
R4 = $k_{\alpha,\beta}\ OM^{\alpha,\beta}\ \left(\frac{[Fe(OH)_3]}{K_{m,Fe(OH)_3}+[Fe(OH)_3]}\right)\left(\frac{[MnO_2]}{K_{m,MnO_2}+[MnO_2]}\right)\left(\frac{[NO_3^-]}{K_{m,NO_3^-}+[NO_3^-]}\right)\left(\frac{[O_2]}{K_{m,O_2}+[O_2]}\right)$	E4
R5 = $k_{\alpha,\beta}\ OM^{\alpha,\beta}\left(\frac{[SO_4^{2-}]}{K_{m,SO_4^{2-}}+[SO_4^{2-}]}\right)\left(\frac{[Fe(OH)_3]}{K_{m,Fe(OH)_3}+[Fe(OH)_3]}\right)\left(\frac{[MnO_2]}{K_{m,MnO_2}+[MnO_2]}\right) * \left(\frac{[NO_3^-]}{K_{m,NO_3^-}+[NO_3^-]}\right)\left(\frac{[O_2]}{K_{m,O_2}+[O_2]}\right)$	E5

R6 = $$k_{\alpha,\beta}\ \mathrm{OM}^{\alpha,\beta}\left(\frac{K_{m,\mathrm{SO_4^{2-}}}}{K_{m,\mathrm{SO_4^{2-}}}+[\mathrm{SO_4^{2-}}]}\right)\left(\frac{[\mathrm{Fe(OH)_3}]}{K_{m,\mathrm{Fe(OH)_3}}+[\mathrm{Fe(OH)_3}]}\right)\left(\frac{[\mathrm{MnO_2}]}{K_{m,\mathrm{MnO_2}}+[\mathrm{MnO_2}]}\right) * \left(\frac{[\mathrm{NO_3^-}]}{K_{m,\mathrm{NO_3^-}}+[\mathrm{NO_3^-}]}\right)\left(\frac{[\mathrm{O_2}]}{K_{m,\mathrm{O_2}}+[\mathrm{O_2}]}\right)$$	E6
Secondary redox and other reaction equations	
R7 = $k_1\ [\mathrm{O_2}]\ [\mathrm{Fe^{2+}}]$	E7
R8 = $k_2\ [\mathrm{O_2}]\ [\mathrm{FeS}]$	E8
R9 = $k_3\ [\mathrm{O_2}]\ [\mathrm{FeS_2}]$	E9
R10 = $k_4\ [\mathrm{O_2}]\ [\sum \mathrm{H_2S}]$	E10
R11 = $k_5\ [\mathrm{O_2}]\ [\mathrm{CH_4}]$	E11
R12 = $k_6\ [\mathrm{Fe(OH)_3}^{\alpha}]\ [\sum \mathrm{H_2S}]$	E12
R13 = $k_7\ [\mathrm{Fe^{2+}}]\ [\sum \mathrm{H_2S}]$	E13
R14 = $k_8\ [\mathrm{FeS}]\ [\sum \mathrm{H_2S}]$	E14
R15 = $k_9\ [\mathrm{SO_4^{2-}}]\ [\mathrm{CH_4}]$	E15
R16 = $k_{10}\ [\mathrm{Fe(OH)_3}^{\alpha,\beta}][\mathrm{CH_4}]$	E16
R17 = $k_{11}\ [S^0]$	E17
R18 = $k_{12}\ [\mathrm{FeS}]\ [S^0]$	E18
R19 = $k_{13}\ [\mathrm{Fe(OH)_3}^{\alpha}]$	E19
R20 = $k_{14}\ [\mathrm{Fe(OH)_3}^{\beta}]\ [\sum \mathrm{H_2S}]$	E20
R21 = $k_{15}\ [\mathrm{O_2}]\ [\mathrm{NH_4^+}]$	E21
R22 = $k_{16}\ [\mathrm{Fe^{2+}}]\ [\mathrm{HPO_4^{2-}}]$	E22
R23 = $k_{17}\ [\mathrm{Fe^{2+}}]\ [\mathrm{HCO_3^-}]$	E23

R24 = k_{18} $[FeCO_3]$ $[\sum H_2S]$	E24
R25 = k_{19} $[Fe_3(PO_4)_2]$ $[\sum H_2S]$	E25
R26 = k_{20} $[Mn^{2+}]$ $[HCO_3^-]$	E26
R27 = k_{21} $[Mn^{2+}]$ $[O_2]$	E27
R28 = k_{22} $\left[Mn(OH)_4^{\alpha,\beta}\right]$ $[Fe^{2+}]$	E28
R29 = k_{23} $\left[Mn(OH)_4^{\alpha}\right]$ $[\sum H_2S]$	E29
R30 = k_{24} $\left[Mn(OH)_4^{\alpha}\right]$	E30
R31 = k_{25} $\left[Mn(OH)_4^{\beta}\right]$ $[\sum H_2S]$	E31
R32 = k_{26} $\left[Mn(OH)_4^{\alpha,\beta}\right]$ $[CH_4]$	E32
R33 = k_{27} $[Mn^{3+}]$ $[O_2]$	E33
R34 = k_{28} $[Mn^{3+}]$ $[\sum H_2S]$	E34
R35 = k_{29} $[Mn^{3+}]$ $[Fe^{2+}]$	E35
R36 = k_{30} $[CO_2]$ $[H_2]$	E36
R37 = k_{31} $[OM^{\alpha}]$	E37
R38 = k_{32} $[NO_3^-][CH_4]$	E38
R39 = k_{33} $[Mn^{3+}][OM^{\alpha}]$	E39

Table S4. Reaction parameters used in the model

Parameter	Value	Unit	Source	Values in literature
k_{α}*	1.62	yr^{-1}	a, b	0.05 – 1.62
k_{β}*	0.0086	yr^{-1}	b, d	0.0025 - 0.0086
K_{O_2}	20	μmol L^{-1}	c	1 – 30
$K_{NO_3^-}$	20	μmol L^{-1}	c	4 – 80

$K_{Mn(OH)_4}$	32	µmol L^{-1}	c	4 – 32
$K_{Fe(OH)_3}$	65	µmol L^{-1}	c	65 – 100
$K_{SO_4^{2-}}$	1.6	µmol L^{-1}	c	1.6
k_1 (E7)	$1.4*10^5$	mmol yr^{-1}	c	$1.4*10^5$
k_2 (E8)	300	mmol yr^{-1}	c	300
k_3 (E9)	1	mmol yr^{-1}	c	1
k_4 (E10)	160	mmol yr^{-1}	c	160
k_5 (E11)	100	mmol yr^{-1}	c	107
k_6 (E12)	80	mmol yr^{-1}	c, g, i	8 - 100
k_7 (E13)	11840	mmol yr^{-1}	b, d	100 - 14800
k_8 (E14)	0.0003	mmol yr^{-1}	e, i	0.0003 – 0.0074
k_9 (E15)	1.344	mmol yr^{-1}	c, g	10 (c) – 120 (g)
k_{10} (E16)	$3.04*10^{-6}$	mmol yr^{-1}	g, i	$1.6*10^{-7}$ – 0.0074
k_{11} (E17)	3	yr^{-1}	f	3
k_{12} (E18)	0.1	mmol yr^{-1}	f, g	0.001 - 7
k_{13} (E19)	0.1	yr^{-1}		model constrained
k_{14} (E20)	0.444	mmol yr^{-1}	c, j	0.004 – 100
k_{15} (E21)	19500	mmol yr^{-1}	c, d	5000 – 39000
k_{16} (E22)	0.052	mmol yr^{-1}		model constrained
k_{17} (E23)	0.000351	mmol yr^{-1}	i	0.0027
k_{18} (E24)	0.0008	mmol yr^{-1}		model constrained
k_{19} (E25)	$8*10^{-4}$	mmol yr^{-1}	i	$8*10^{-4}$
k_{20} (E26)	0.05565	mmol yr^{-1}	k	0.265
k_{21} (E27)	15000	mmol yr^{-1}	c	800 - 20000
k_{22} (E28)	2.652	mmol yr^{-1}	f, k	0.002 - 2
k_{23} (E29)	1	mmol yr^{-1}	c	< 100000 (20)
k_{24} (E30)	1.8	yr^{-1}	f	1.8
k_{25} (E31)	0.02	mmol yr^{-1}	c	< 100000 (20)
k_{26} (E32)	0.000019	mmol yr^{-1}	k	0.0017
k_{27} (E33)	144	mmol yr^{-1}		model constrained
k_{28} (E34)	64	mmol yr^{-1}		model constrained

k_{29} (E35)	0.025	mmol yr^{-1}		model constrained
k_{30} (E36)	0.03675	yr^{-1}		model constrained
k_{31} (E37)	0.15	yr^{-1}		model constrained
k_{32} (E38)	0.5	mmol yr^{-1}		model constrained
k_{33} (E39)	$2.5*10^{-4}$	mmol yr^{-1}		model constrained

a) Moodley et al. (2005); b) Reed et al. (2011a) c) Van Cappellen & Wang (1996); d) Reed et al. (2016); e) Rickard (1997); f) Berg et al. (2003); g) Rooze et al. (2016); h) Egger et al. (2016a); i) Egger et al. (2016b); j) Lenstra et al. (2018)

*****Following the approach of Reed et al. (2011b), we have assumed different reactivities of the organic matter towards the electron acceptors. The following factors have been used for the α fraction: O_2 = 1, NO_3 = 3, MnO_2 = 2.8, $Fe(OH)_3$ = 0.3, SO_4^{2-} = 1.7, methanogenesis = 0.5; for the β fraction the following factors have been used: O_2 = 1, NO_3^- = 3, MnO_2 = 1, $Fe(OH)_3$ = 0.3, SO_4^{2-} = 1, methanogenesis = 3.

Table S5. Environmental parameters used in the model. Values of porosity, temperature, salinity and the sedimentation rate are based on data for the study site.

Parameter	Symbol	Value	Unit
Porosity at surface	ϕ_0	0.944	vol/vol
Porosity at depth	ϕ_∞	0.888	-
Porosity e-folding distance	g	60	cm
Sediment density	r	2.65	g cm^{-3}
Temperature	T	8.4	˚C
Salinity	S	35	-
Pressure	P	5.5	bar
Tortuosity	q^2	$1 - 2\ln(\phi)$	-
Molecular diffusion coefficient corrected for tortuosity	D'	$D' = \frac{D_m}{\theta^2}$	cm^{-2} yr^{-1}
Sediment accumulation rate**	F_{Sed}	**	g cm^{-2} yr^{-1}
Advective velocity at surface	n_0	$\frac{F_{sed}}{\rho(1-\varphi_0)}$	cm yr^{-1}

Advective velocity at depth	n_∞	$\frac{F_{sed}}{\rho(1-\varphi_\infty)}$	cm yr^{-1}

** Sedimentation rate variations over the years			
Year	December – July	July - December	Unit
0 – 60	2.97	2.97	g cm^{-2} yr^{-1}
60 – 75	0.69	3.93	g cm^{-2} yr^{-1}
75 – 80	3.93	2.00	g cm^{-2} yr^{-1}

Table S6. The various diffusion coefficients used for Mn(III) ($D_{Mn(III)}$) to evaluate the effect of the choice of the diffusion coefficient for Mn(III) when it forms a complex with an organic ligand.

Name	Scenario	Value	Range in literature	Sources
High $D_{Mn(III)}$	DMn(III) = DMn(II) As calculated by reactran package	132.6 cm^2 yr^{-1}	-	*a*
Middle $D_{Mn(III)}$	DMn(III) is within the range of diffusion coefficients for dissolved organic matter	33.1 cm^2 yr^{-1}	22.7 – 81 cm^2 yr^{-1}	*b, c*
Low $D_{Mn(III)}$	DMn(III) is constrained by the model, by fitting Mn(III) to the collected data. This is the DMn(III) that is used in the model throughout the paper.	16.6 cm^2 yr^{-1}	-	

Sources: *a*) Soetaert & Meysman (2012); *b*) Burdige et al. (1999); *c*) Burdige et al. (2004)

115

Table S7. Boundary conditions of solids and solutes at the sediment-water interface in the model. For the time-dependent fluxes of $OM^{\alpha,\beta,\gamma}$, $Fe(OH)_3{}^{\alpha,\beta,\gamma}$, $MnO_2{}^{\alpha,\beta}$ and $MnCO_3$ and concentration of O_2 the minimum and maximum fluxes and concentrations are given. For all chemical species, a zero-gradient boundary condition was specified at the bottom of the model domain.

Solids	**Flux at sediment-water interface**		**Unit**
FeS	$0.4 * 10^{-4}$		mol m^{-2} yr^{-1}
FeS_2	0		mol m^{-2} yr^{-1}
S^0	0		mol m^{-2} yr^{-1}
$FeCO_3$	2		mol m^{-2} yr^{-1}
$Fe_3(PO_4)_2$	0		mol m^{-2} yr^{-1}
	Min	**Max**	
OM^a	9.51	52.31	mol m^{-2} yr^{-1}
OM^b	45.36	72.58	mol m^{-2} yr^{-1}
OM^g	0.001	0.001	mol m^{-2} yr^{-1}
$Fe(OH)_3{}^a$	0.0028	6.44	mol m^{-2} yr^{-1}
$Fe(OH)_3{}^b$	3.28	4.68	mol m^{-2} yr^{-1}
$Fe(OH)_3{}^g$	0	0	mol m^{-2} yr^{-1}
$MnO_2{}^a$	0.0108	0.081	mol m^{-2} yr^{-1}
$MnO_2{}^b$	0.0235	0.216	mol m^{-2} yr^{-1}
$MnCO_3$	0.0624	0.163	mol m^{-2} yr^{-1}
Solutes	**Bottom water concentrations**		**Unit**
	Min	**Max**	
O_2	0	0.205	mmol L^{-1}
ΣH_2S	0	0.111	mmol L^{-1}
Cl^-	532		mmol L^{-1}
$NO_3{}^-$	0		mmol L^{-1}
$SO_4{}^{2-}$	27.49		mmol L^{-1}
CH_4	0		mmol L^{-1}
Fe^{2+}	0		mmol L^{-1}
$\Sigma NH_4{}^+$	0		mmol L^{-1}
$\Sigma HPO_4{}^{2-}$	0		mmol L^{-1}
DIC	3		mmol L^{-1}
Mn^{2+}	0		mmol L^{-1}

Mn^{3+}	0	mmol L^{-1}

References

Berg, P., Rysgaard, S., & Thamdrup, B. O. (2003). Dynamic Modeling of Early Diagenesis and Nutrient Cycling. A Case Study in an Arctic Marine Sediment. *American Journal of Science*, *303*, 905–955.

Boudreau, B. P. (1997). *Diagenetic models and their implementation : modelling transport and reactions in aquatic sediments Modelling Transport and Reactions in Aquatic Sediments*. Springer Berlin Heidelberg. https://doi.org/10.1007/978-3-642-60421-8

Boudreau, P. (1996). A Method-of-Lines Code For Carbon and Nutrient Diagenesis in Aquatic Sediments. *Computers & Geoscience*, *22*(5), 479–496.

Burdige, D. J., Berelson, W. M., Coale, K. H., McManus, J., & Johnson, K. S. (1999). Fluxes of dissolved organic carbon from California continental margin sediments. *Geochimica et Cosmochimica Acta*, *63*(10), 1507–1515.

Burdige, D. J., Kline, S. W., & Chen, W. (2004). Fluorescent dissolved organic matter in marine sediment pore waters. *Marine Chemistry*, *89*, 289–311. https://doi.org/10.1016/j.marchem.2004.02.015

Egger, M., Kraal, P., Jilbert, T., Sulu-gambari, F., Sapart, C. J., & Röckmann, T. (2016a). Anaerobic oxidation of methane alters sediment records of sulfur , iron and phosphorus in the Black Sea. *Biogeosciences*, 5333–5355. https://doi.org/10.5194/bg-13-5333-2016

Egger, M., Lenstra, W., Jong, D., Meysman, F. J. R., Sapart, C. J., Van Der Veen, C., Röckmann, T., Gonzalez, S., & Slomp, C. P. (2016b). Rapid sediment accumulation results in high methane effluxes from coastal sediments. *PLoS ONE*, *11*(8), 1–22. https://doi.org/10.1371/journal.pone.0161609

Froelich, P. N., Klinkhammer, G. P., Bender, M. L., Luedtke, N. A., Heath, G. R., Cullen, D., Dauphin, P., Hammond, D., & Hartman, B. (1979). Early oxidation of organic matter in pelagic sediments of the eastern equatorial Atlantic : suboxic diagenesis. *Geochimica et Cosmochimica Acta*, *43*, 1075–1090.

Lenstra, W. K., Egger, M., Helmond, N. A. G. M. Van, Kritzberg, E., & Conley, D. J. (2018). Large variations in iron input to an oligotrophic Baltic Sea estuary : impact on sedimentary phosphorus burial. *Biogeosciences*, 6979–6996.

Meysman, F. J. R., Boudreau, B. P., & Middelburg, J. J. (2005). Modeling reactive transport in sediments subject to bioturbation and compaction. *Geochimica et Cosmochimica Acta*, *69*(14), 3601–3617. https://doi.org/10.1016/j.gca.2005.01.004

Moodley, L., Middelburg, J. J., Herman, P. M. J., Soetaert, K., & de Lange, G. J. (2005). Oxygenation and organic-matter preservation in marine sediments : Direct experimental evidence from ancient organic carbon – rich deposits. *Geology*, *11*, 889–892. https://doi.org/10.1130/G21731.1

Reed, D. C., Gustafsson, B. G., & Slomp, C. P. (2016). Shelf-to-basin iron shuttling enhances vivianite formation in deep Baltic Sea sediments. *Earth and Planetary Science Letters*, *434*, 241–251. https://doi.org/10.1016/j.epsl.2015.11.033

Reed, D. C., Slomp, C. P., & de Lange, G. J. (2011a). A quantitative reconstruction of organic matter and nutrient diagenesis in Mediterranean Sea sediments over the Holocene. *Geochimica et Cosmochimica Acta*, *75*(19), 5540–5558.

https://doi.org/10.1016/j.gca.2011.07.002

Reed, D. C., Slomp, C. P., & Gustafsson, B. G. (2011b). Sedimentary phosphorus dynamics and the evolution of bottom-water hypoxia: A coupled benthic-pelagic model of a coastal system. *Limnology and Oceanography*, *56*(3), 1075–1092. https://doi.org/10.4319/lo.2011.56.3.1075

Rickard, D. (1997). Kinetics of pyrite formation by the H2S oxidation of iron (II) monosulfide in aqueous solutions between 25 and 125 ° C : The rate equation. *Geochimica et Cosmochimica Acta*, *61*(1), 115–134.

Rooze, J., Egger, M., Tsandev, I., & Slomp, C. P. (2016). Iron-dependent anaerobic oxidation of methane in coastal surface sediments: Potential controls and impact. *Limnology and Oceanography*, *61*(1), S267–S282. https://doi.org/10.1002/lno.10275

Soetaert, K., & Meysman, F. (2012). Environmental Modelling & Software Reactive transport in aquatic ecosystems : Rapid model prototyping in the open source software R. *Environmental Modelling and Software*, *32*, 49–60. https://doi.org/10.1016/j.envsoft.2011.08.011

Soetaert, K., Petzoldt, T., & Meysman, F. (2010). *marelac : Tools for Aquatic Sciences*.

Van Cappellen, P., & Wang, Y. (1996). Cycling of iron and manganese in surface sediments: a general theory for the coupled transport and reaction of carbon, oxygen, nitrogen, sulfur, iron and manganese. *American Journal of Science*, *296*(March), 197–243.

Żygadłowska, O. M., Venetz, J., Klomp, R., Lenstra, W. K., Van Helmond, N. A. G. M., Röckmann, T., Wallenius, A. J., Dalcin Martins, P., Veraart, A. J., Jetten, M. S. M., & Slomp, C. P. (2023). Pathways of methane removal in the sediment and water column of a seasonally anoxic eutrophic marine basin. *Frontiers in Marine Science*, *January*, 1–15. https://doi.org/10.3389/fmars.2023.1085728